Master of Science Thesis
VT2015

Indirect detection of myelin water by T2-relaxation during the RF pulse

Yosef Al-Abasse

Supervision

Gunther Helms, Lund

Department of Medical Radiation Physics,
Clinical Sciences, Lund
Lund University
www.msf.lu.se

Abstract

Introduction: The axonal myelin sheath is the main cause of magnetic resonance imaging (MRI) contrast between gray matter (GM) and white matter (WM) in the brain. It encloses a small pool of myelin water (MW) with a short T_2 of about 15 ms. Common signal equations of MRI sequence assume an instantaneous RF excitation pulse followed by free relaxation. As known from ultra-short echo time (UTE) MRI, deviations from this signal behavior may occur when the relaxation times are shorter than or of the same order of magnitude as the duration of radio frequency (RF) excitation pulse. In this MSc thesis project, it was studied whether such transverse in-pulse relaxation effects can be used to detect MW by increasing the RF pulse duration to the range of the MW T_2. By such an approach, the in-pulse relaxation effects, which alter the MRI signal, would arise mainly from MW.

Material and methods: By numerical integration of the Bloch equations, in-pulse relaxation effects on the magnetization were studied for rectangular (RECT), Gaussian and sinc-shaped (SINC) pulses of 10 ms pulse duration in order to find the optimal RF pulse for imposing different degrees of saturation onto the longitudinal magnetizations of MW and intra–/extra-axonal water with optimal excitation profile, i.e., minimal degradation in the signal intensities. The effect of longitudinal relaxation during the RF pulse was neglected because T_1 of MW and intra– and extra-axonal water (IE-water) is much longer than the duration of the RF pulse. The fast low angle shot (FLASH) pulse sequence of a 3 T MR scanner (Siemens Magnetom Skyra) was modified to provide two pulse durations of 0.5 ms and 10 ms using a Gaussian RF pulse. FLASH MRI at variable flip angles was carried out on three cream phantoms (12 %, 27 % and 40 % fat content), a formalin-fixated pig brain and a healthy volunteer. The measurement with short pulse duration served as a reference to the difference in apparent T_1.

Results: The simulations indicated that in-pulse relaxation would result in a reduced partial saturation of MW magnetization which is largely independent on flip angle and amounting to between 6 % (SINC) and 21 % (RECT). A Gaussian shape (11 % reduced partial saturation) was implemented experimentally, as this shape was less sensitive to frequency offsets, due to the shape of the excitation profile, than the RECT. With the long pulse, the apparent T_1 was about 25 % shorter in WM and 10 % shorter in GM, for both the fixated brain and in vivo, and the effects were thus much larger than expected from the simulations. The spatial distribution of the T_1 reduction showed more pronounced reduction in the WM, where MW is localized. The simulations for the cream phantoms indicated a halving of the in-pulse relaxation effects compared with the MW and IE-water in vivo, and thus no mapping of the apparent T_1 was performed.

Conclusion: The reference measurement was most likely affected by magnetization transfer (MT) effects from macromolecules, for which saturation is also influenced by RF pulse duration. Thus, the shorter the pulse duration, the more the MT effects are pronounced. Compared with in-pulse relaxation effects, the MT effects seemed to be dominating, and further studies are needed to separate these effects.

Summary in Swedish

Magnetkameran är en icke-invasiv metod som används för att avbilda mjukvävnad i kroppen med hög spatial upplösning. Myelinskidan som omger axonerna i det centrala nervsystemet ger upphov till kontrasten mellan vit och grå substans i konventionella magnetkamerabilder. Det är av intresse att detektera nedbrytningen av myelinskidan eftersom förekomst av sådan kan ge en indikation på tidigare stadier av den neurologiska sjukdomen multipel skleros (MS). Idag finns det utmaningar inom magnetresonansfysiken (MR-fysiken) vid direkt detektering av myelinskidan eftersom signalen från den avtar på några få mikrosekunder. En radiofrekvent (RF) puls används för att flippa ned magnetiseringsvektorn till det transversella planet och därmed generera MR signalen. I konventionell signalbeskrivning antas att RF-pulsen appliceras momentant, och är direkt följd av fri relaxation. MR-signalen som erhållits med en konventionell (d.v.s. kort) RF-puls är inte selektivt känslig för myelin-vatten utan består av signal från både myelin-vatten och intra– och extra cellulärt vatten (IE-vatten). Dessutom är valet av RF-pulsen avgörande, eftersom olika RF-pulser innehar olika egenskaper som potentiellt kan användas för att urskilja de två populationerna. I detta arbete förlängdes RF-pulsen till 10 ms för att kunna separera dessa två populationer genom skillnader i den transversella relaxationen, T_2. Myelin-vattnet relaxerar snabbare ($T_{2,\text{myelin vatten}} \approx 15$ ms) än IE-vatten ($T_{2,\text{IE-vatten}} \approx 80$ ms). Som en följd av detta kan relaxationseffekterna under den långa RF-pulsen inte försummas, vilket leder till att den klassiska signalekvationen måste modifieras. Effekter från den longitudinella relaxationen försummades eftersom T_1 antogs vara mycket längre än RF-pulsen. Som referens användes mätning med kort RF-puls (0,5 ms) i denna studie. För att erhålla robusta mätresultat genererades en skenbar T_1-karta med den långa RF-pulsen, och denna jämfördes sedan med motsvarande skenbara T_1-karta för den korta RF-pulsen. Den resulterande bilden avslöjade var den största skillnaden mellan de skenbara T_1-kartorna fanns, och denna skillnad antogs bero på relaxationseffekter hos myelin-vattnet.

Den ovan beskrivna metoden användes i detta arbete med en Gaussisk puls som testades på tre olika gräddfantom med olika fetthalter (12 %, 27 % och 40 %), på formalinfixerad grishjärna samt i en volontär. Den resulterade differensen i $T_{1,\text{skenbart}}$ mellan kort och lång puls visade en observerad effekt på 25 % i vit substans och 10 % i grå substans. Denna effekt var mycket högre än vad simuleringar av Bloch-ekvationerna antydde (d.v.s. 11 %). Magnetiseringsöverföringseffekter (magnetization transfer, MT) från makromolekyler influerade troligen mätningen med den korta RF-pulsen. MT-effekterna blir större ju kortare RF-pulsen blir. Således beror MT-effekterna på pulslängden och detta studerades inte i denna studie. Detta medförde att den stora observerade effekten på differensen i $T_{1,\text{skenbart}}$ troligen dominerades av MT. Det krävs därför ytterligare studier, med varierad pulslängd, för att kunna separera dessa två effekter.

Abbreviations

Diffusion tensor imaging	DTI
Echo time	TE
Fast low angle shot	FLASH
Field of view	FOV
Flip angle	FA
Full width at half maximum	FWHM
Grey matter	GM
Intra– and extra-axonal water	IE-water
Inversion time	IR
Magnetic resonance imaging	MRI
Magnetization transfer	MT
Myelin water	MW
Myelin water fraction	MWF
Nuclear magnetic resonance	NMR
Partial saturation degree	PSD
Radio frequency	RF
Rectangular	RECT
Region of interest	ROI
Repetition time	TR
Variable flip angle	VFA
White matter	WM

Table of contents

1. Introduction

Magnetic resonance imaging (MRI) is a non-invasive technique for diagnostic imaging of soft tissue with high spatial resolution [1]. The brain and spine central nervous system consists mainly of glia cells and neurons. The glia cells are non-neuronal cells that form the myelin, and additionally contribute to protection and support for the neurons. The myelin causes the whitish appearance of white matter (WM) of the brain. The main function of the neurons is to receive and transmit information via the axon, which can be wrapped in myelin sheaths, leading to accelerated impulses, unlike the impulses via the unmyelinated axons in grey matter (GM).

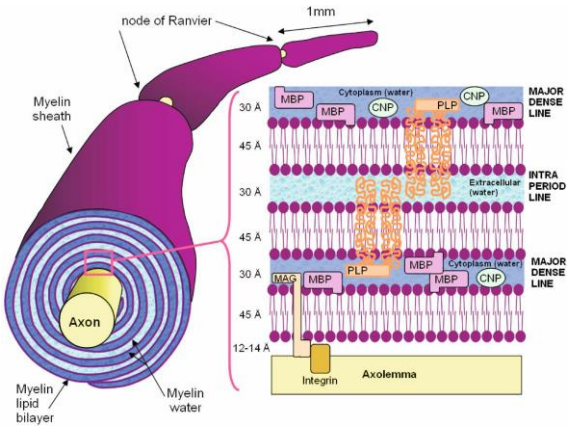

Figure 1: Schematic image of myelin sheath wrapped around an axon with a zoomed image of the myelin bilayer. The abbreviations in the zoomed image are different types of proteins. The nodes of Ranvier are located between every two adjacent myelin sheaths [2].

As shown in the figure above, the myelin membrane consists of alternating bilayers of proteins and lipids. The permeability of multiple myelin membranes lowers the exchange of water, so the myelin water (MW) trapped inside the sheaths forms a separate compartment with bound water. The compartments of intra– and extra-axonal water (IE-water) cannot be discerned by the transverse relaxation time, T_2, and in MRI they are thus considered as a single compartment of bulk water with less restriction. The MW has a short T_2 of 15 ms due to the cross-relaxation by dipole-dipole interaction with rotationally hindered protons [3]. Furthermore, the myelin has a short longitudinal relaxation time, T_1, and the lipid protons do not contribute to the MR signal [4]. Therefore, the MR signal of WM is described by two compartments with exchange, MW and IE-water [5].

It is of considerable interest to detect the myelin sheath, and thereby discovering loss of myelin, which among other mechanisms, characterizes autoimmune disease of the central nervous system, i.e., multiple sclerosis (MS) [6]. Unfortunately, it is very difficult to image the myelin directly, owing to the rapidly decaying signal, about tens of µs, and the indistinguishable MR signal that arises from proteins and lipids in the myelin– from non-myelin tissue [7]. Hence, challenges with direct methods, such as the ultra-short echo time (UTE) imaging [8] exist, mainly in eliminating the mixed signal from MW.

Myelin can be detected indirectly by different MRI techniques such as conventional T_1/T_2-weighted imaging, diffusion tensor imaging (DTI), magnetization transfer (MT) imaging and separation of T_2 relaxation components [3]. Conventional T_1/T_2-weighted imaging is mainly

applicable to children younger than 2 years. This is the age when most of the myelination takes place, which leads to changes in the relaxation times [9]. This method has a low specificity because other reasons than myelination can also cause changes in the relaxation times, and the method has low sensitivity when studying objects > 2 years old. DTI measures the thermal motion of water molecules. According to animal studies [10, 11], loss of myelin implies an increased radial diffusivity, indicating a relationship between DTI parameters and myelin. Unfortunately, the fiber tract orientation, and hence the radial diffusivity is difficult to determine in regions where the anisotropy is low, for example, crossing fibers. This implicates that the small changes in radial diffusivity are not detected [12]. The MT ratio is a measure of the exchange between the bulk water and macromolecules in tissue, which is well known for its technical simplicity and sensitivity to lesions [6]. This parameter, on the other hand, suffers from low specificity because it is affected by, for example, changes in water content and T_1 as well as in myelination [13]. Another method to detect the myelin indirectly is based on the collection of MR signal at several echo times (TEs). Advanced post-processing is needed to separate the two T_2 components, i.e., short T_2 belonging to MW and long T_2 belonging to IE-water [3]. Thus, the myelin content is described by the so-called myelin water fraction (MWF). On the other hand, decreased MWF, and thus higher water content, can be caused by edema or inflammation, and the method is not a specific measure of myelination [14].

The MW and IE-water have different transverse relaxation times, i.e., 15 ms and 80 ms, respectively, [3]. Conventionally, the fast low angle shot (FLASH) signal equation assumes radio-frequency (RF) pulses to be applied instantaneously at the center of the actual pulse duration, immediately followed by free relaxation [15]. The approach proposed in this MSc thesis to detect the MW indirectly is based on increasing the RF pulse duration to the range of the myelin transverse relaxation time. Such long RF pulses can be regarded as “discriminant” of MW because the T_2 relaxation effects during the RF pulse, the so called in-pulse relaxation, can no longer be neglected, whereas the effect of longitudinal relaxation during the RF pulse can be neglected because the T_1 of MW and IE-water is much longer than the duration of the RF pulse. Hence, the regular Ernst signal equation [16] used in the variable flip angle (VFA) method to enable mapping of apparent T_1 with the long RF pulse becomes invalid [15]. To obtain differences in the apparent T_1 map between the two populations, the RF pulse should impose different degrees of saturation based on MW alone. Therefore, pixel-wise comparison between the apparent T_1 maps belonging to the long and short pulses, respectively, would give a difference in apparent T_1 that is influenced by the in-pulse relaxation of the MW. The aim of this study was to find, implement and test “discriminant” RF excitation pulses expected to impose different saturation degrees between MW and IE-water with optimal excitation profile, i.e., the Fourier transform of the time dependent RF pulse shape that determines the width, uniformity and phase of the excited frequency range. Such an excitation profile provides minimal degradation in the signal intensities, and thereby avoiding a bias and increased variance in the measured T_1. The pulse sequence used here was a FLASH in order to enable VFA T_1 measurements. Experiments were performed in vitro using dairy cream phantoms with different fat contents, because of the exhibition of multicomponent relaxation times similar to that in WM [17]. An ex vivo pig brain prepared in formalin, with shorter measured longitudinal and transverse relaxation times than the brain in vivo, was also used with the aim to observe the in-pulse relaxation effects. These in vitro effects were expected to be more pronounced than in an in vivo subject owing to the relatively short relaxation times of the pig brain. Finally, an in vivo brain measurement was performed in a healthy volunteer.

2. Theory

2.1 Physical background of the MRI signal

A typical MRI signal is generated from the magnetic moment of the hydrogen nucleus. According to quantum physics, the spin of the proton is an inherent property, representing the internal angular momentum. In terms of a classical physics analogy, the proton, which is a charged particle, is spinning about its own axis, and thus acting as a magnetic dipole that exhibits a magnetic moment. In presence of an external magnetic field, the spins are aligned parallel with or antiparallel to it. According to the Boltzmann distribution, the lowest energy state for protons corresponds to alignment parallel with the external magnetic field, and this energy state thus has the largest proton population at thermal equilibrium. For quantum mechanical reasons, the protons are not oriented exactly parallel or antiparallel with the external field but at a slight angle, which will create a torque on the protons. The net effect is to create a magnetization vector with the same direction as the external magnetic field. The effect of the exerted torque is to rotate any component of the magnetic moment in the transverse plane around the external magnetic field, giving rise to a precession phenomenon. The precession is occurring with an angular frequency, ω_0, known as the Larmor frequency or resonance frequency [18], which is given by

$$\omega_0 = \gamma B_0, \tag{1}$$

where γ is the gyromagnetic ratio of $2.67 \cdot 10^8 \text{ rad s}^{-1} T^{-1}$ for protons and B_0 is the external magnetic flux density. When exposing the spins to an RF pulse with a frequency equal to the precession frequency of the protons (i.e., the resonance frequency), net absorption of RF-energy by the protons occurs, and they are elevated to a higher energy state. As a result of this disruption of the equilibrium state, the net magnetization vector is rotated from the z or B_0 direction to the transverse plane, xy-plane, which is perpendicular to B_0. The subsequent rotation of magnetization in the xy-plane leads to an induction of voltage in a coil placed around the object according to the Faraday induction law. Simply expressed, the MR signal is amplified from the electrical current produced.

2.2 Bloch equations

The Bloch equations describe the macroscopic magnetization vector, **M**, in x, y and z-direction as a function of time with respect to the excitation by an RF pulse and to relaxation described by time constants T_1 and T_2 [18]. The process describing the recovery of longitudinal magnetization, M_z, to thermal equilibrium magnetization, M_0, is called T_1 relaxation. The process describing the decay of the M_{xy} component or dephasing of spins is called T_2 relaxation. Variations in magnetic susceptibility between materials of different composition can lead to magnetic field inhomogeneities near tissue interfaces and associated dephasing of spins. When taking into account the inhomogeneities in the static magnetic field, the transverse relaxation is called T_2^* relaxation. The relaxation processes occur simultaneously with the condition $T_2^* \leq T_2 \leq T_1$.

In the z-direction, **M** is constant at equilibrium, which means:

$$\frac{d\mathbf{M}_z(t)}{dt} = 0 \tag{2}$$

The magnetizations in the x –and y-directions show precession about B_0 at the Larmor frequency and can be described as follows

$$\frac{d\mathbf{M}_x(t)}{dt} = \gamma \mathbf{M}_y \mathbf{B_0} \tag{3}$$

$$\frac{d\mathbf{M}_y(t)}{dt} = -\gamma \mathbf{M}_x \mathbf{B_0} \tag{4}$$

The exciting RF-field, $2B_{1\max} \cdot \cos(\omega t)$, can be split into two rotating components in opposite directions, where the angular frequencies are $\pm\omega$. The time-varying magnetic field, $B_1(t)$, that is created when irradiating with an RF-pulse, can arbitrary be chosen along x-axis.

When combining the effects of $\mathbf{B_0}$ and the exciting magnetic field, $\mathbf{B_1}(t)$ on the three components, x, y and z, the following equations result

$$\frac{d\mathbf{M}_x(t)}{dt} = \gamma\left[\mathbf{M}_y(t)\mathbf{B_0} - \mathbf{M}_z(t)\mathbf{B_1}\sin(\omega t)\right] \tag{5}$$

$$\frac{d\mathbf{M}_y(t)}{dt} = \gamma\left[\mathbf{M}_z(t)\mathbf{B}_1\cos(\omega t) - \mathbf{M}_x(t)\mathbf{B}_0\right] \tag{6}$$

$$\frac{d\mathbf{M}_z(t)}{dt} = \gamma\left[\mathbf{M}_x(t)\mathbf{B}_1\sin(\omega t) - \mathbf{M}_y(t)\mathbf{B}_1\cos(\omega t)\right] \tag{7}$$

The equations above do not take relaxation processes into account for the respective component. The Bloch equations, can however, be modified to include the relaxation processes according to the equations below

$$\frac{d\mathbf{M_x}(t)}{dt} = \gamma\left[\mathbf{M}_y(t)\mathbf{B_0} - \mathbf{M}_z(t)\mathbf{B_1}\sin(\omega t)\right] - \frac{\mathbf{M_x}(t)}{T_2} \tag{8}$$

$$\frac{d\mathbf{M}_y(t)}{dt} = \gamma\left[\mathbf{M}_z(t)\mathbf{B}_1\cos(\omega t) - \mathbf{M}_x(t)\mathbf{B}_0\right] - \frac{\mathbf{M}_y(t)}{T_2} \tag{9}$$

$$\frac{d\mathbf{M}_z(t)}{dt} = \gamma\left[\mathbf{M}_x(t)\mathbf{B}_1\sin(\omega t) - \mathbf{M}_y(t)\mathbf{B}_1\cos(\omega t)\right] - \frac{\mathbf{M}_z(t) - \mathbf{M_0}}{T_1} \tag{10}$$

2.2.1 Bloch equations in the rotating frame of reference

Above, the Bloch equations were described in the laboratory frame of reference. It is often favorable to express the Bloch equations in the rotating frame of reference. Thus, a new Cartesian set of axes will be used, x′, y′ and z′, which rotates about $\mathbf{B_0}$ with frequency ω and with z′ (=z) parallel to $\mathbf{B_0}$. In the rotating frame of reference, the magnetization components are given by

$$\mathbf{M}_x^{'} = \mathbf{M}_{\mathbf{x}} \cos(\omega t) - \mathbf{M}_y \sin(\omega t) \tag{11}$$

$$\mathbf{M}_y^{'} = \mathbf{M}_{\mathbf{x}} \sin(\omega t) + \mathbf{M}_y \cos(\omega t) \tag{12}$$

$$\mathbf{M}_z^{'} = \mathbf{M}_z \tag{13}$$

The Bloch equations in the rotating frame of reference can be calculated [19] using Equations 8-13, which gives

$$\frac{d\mathbf{M}_x^{'}(t)}{dt} = \Delta\omega \mathbf{M}_y^{'}(t) - \frac{\mathbf{M}_x^{'}(t)}{T_2} \tag{14}$$

$$\frac{d\mathbf{M}_{\ddot{y}}^{'}(t)}{dt} = -\Delta\omega \mathbf{M}_x^{'}(t) + \omega_1 \mathbf{M}_z^{'}(t) - \frac{\mathbf{M}_y^{'}(t)}{T_2} \tag{15}$$

$$\frac{d\mathbf{M}_z^{'}(t)}{dt} = -\omega_1 \mathbf{M}_y^{'}(t) - \frac{\mathbf{M}_z^{'}(t) - \mathbf{M}_0}{T_1} \tag{16}$$

where $\omega_1 = \gamma B_1$ is the angular velocity associated with the RF pulse with frequency ω_1, applied along the x′-axis of the rotating frame of reference, $\Delta\omega$ is the frequency offset, i.e., the difference between the Larmor frequency and ω_1.

2.3 RF pulses

The RF pulse is a time dependent magnetic field along arbitrary direction in the xy-plane. An RF pulse is used in nuclear magnetic resonance (NMR) to manipulate the dipole moments, for instance, through spin excitation, inversion or refocusing. After irradiation with an on-resonance RF pulse with the time-varying magnetic field, $\mathbf{B}_1(t)$, the flip angle (FA), α, of the longitudinal magnetization can be expressed as below

$$\alpha = \gamma \cdot \int_0^{T_{RF}} B_1(t) dt\,, \tag{17}$$

where T_{RF} is the pulse length.

RF pulses with constant amplitude are called RECT pulses and are used, for example, to obtain excitations with broad bandwidth so the spins with a wide range of resonant frequencies are affected. Typically, RECT pulses are used for non-slice selective excitations. In some cases, the spins are manipulated using selective RF pulse, which means that instead of excitation of all frequencies, a specific frequency range is excited. Examples of such RF pulses are truncated sinc-shaped– (SINC) and Gaussian pulses.

Note that the RF pulses presented below have different amplitudes to maintain the same integral. This indicates that the RECT pulse has a lower integrated power than a Gaussian pulse which, in turn, has a lower power than a SINC pulse of the same length.

2.3.1 RECT pulse

A RECT pulse has the shape of a step function (Figure *2*).

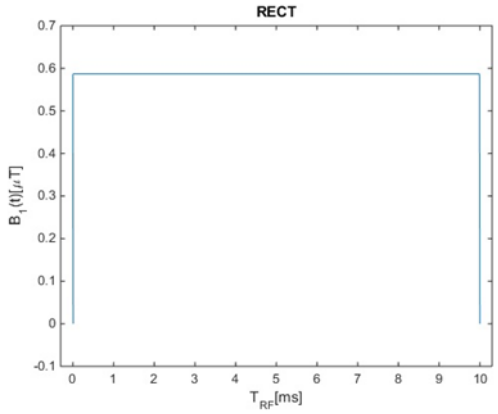

Figure 2: A step function with 10 ms duration.

In the case of no existing off-resonance effects, α for the RECT pulse is given by

$$\alpha = \gamma B_1 T_{RF} \tag{18}$$

2.3.2 Gaussian pulse

The shape of a truncated Gaussian RF pulse is shown in Figure 3 below.

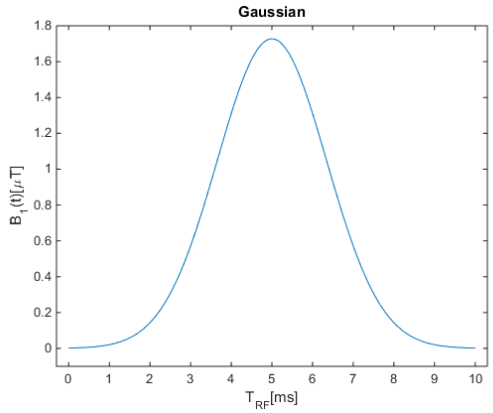

Figure 3: A Gaussian function with 10 ms duration.

The $B_1(t)$ waveform for a Gaussian pulse centered at $t = T_{RF}/2$ is expressed as following

$$B_1(t) = B_{1\max} e^{-\frac{(t-(T_{RF}/2))^2}{2\sigma^2}}, \tag{19}$$

where T_{RF} is the pulse duration and B_{1max} is the amplitude of the Gaussian pulse.

2.3.3 SINC pulse

Another example of a selective RF pulse is a SINC pulse, i.e., described by the sin(t)/t function. It consists of a central lobe with the highest amplitude, and several side lobes, with decreasing amplitudes, on either side of the central lobe. The width of the central lobe is equal to two times the width of each side lobe.

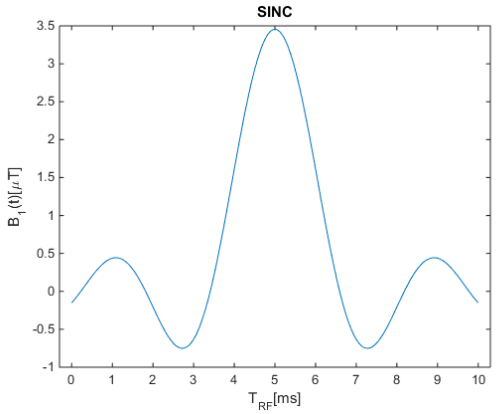

Figure 4: Truncated SINC function with two side lobes and with 10 ms duration.

The SINC function is necessarily truncated due to its infinite duration. The truncation is normally executed at a zero-crossing, which leads to, e.g., "five-lobe" or "seven-lobe" SINC pulses. The time dependent RF shape of a SINC pulse, B_1 (t), is given by

$$B_1(t) = B_{1\max}\ SINC\left(\frac{\pi(t-(T_{RF}/2))}{t_0}\right), \tag{20}$$

where B_{1max} is the peak RF amplitude centered at t = T_{RF}/2 and t_0 is the full width of each side lobe given by

$$t_0 = \frac{T_{RF}}{\sum \#\,\text{lobe widths}} \tag{21}$$

2.4 Fast low-angle shot (FLASH) sequence diagram and signal equation

A MRI pulse sequence is a set of RF pulses, changing magnetic gradients and signal readouts, in a programmed manner. The FLASH sequence is a spoiled gradient echo sequence that eliminates, by RF– and/or gradient spoiling, the steady state transverse magnetization after signal acquisition before the following RF pulse [20]. The sequence diagram for the FLASH-sequence is described in Figure 5 below.

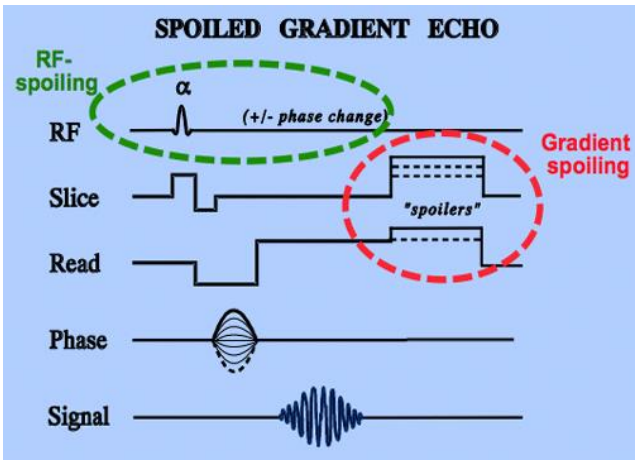

Figure 5: FLASH-sequence timing diagram with RF– and gradient spoiling [21].

In the FLASH sequence, the RF pulse changes the magnetization from M^{-}_{z}, i.e., the steady state of the longitudinal magnetization before the excitation, to M^{+}_{xy}, i.e., the transverse magnetization after the excitation[1].

$$M_{xy}^{+} = M_{z}^{-} \cdot \sin(\alpha) \tag{22}$$

and

$$M_{z}^{+} = M_{z}^{-} \cdot \cos(\alpha) \tag{23}$$

This generates partial saturation, σ, as expressed below

$$\sigma = \frac{M_{z}^{-} - M_{z}^{+}}{M_{z}^{-}} = 1 - \frac{M_{z}^{+}}{M_{z}^{-}} \tag{24}$$

Hence, the higher the FA is, and thus the smaller the M_z^+ component, the higher becomes the partial saturation degree (PSD).

The steady state M_{z}^{-} component is derived from the following condition:

$$M_0 - M_{z}^{-} = (M_0 - M_{z}^{+}) \cdot E_1 = (M_0 - M_{z}^{-} \cdot \cos(\alpha)) \cdot E_1, \tag{25}$$

where $E_1 = e^{-TR/T_1}$ and TR is the repetition time. The equation above leads to the steady state of M_{z}^{-}, i.e.,

$$M_{z}^{-} = M_0 \frac{1 - E_1}{1 - E_1 \cos(\alpha)} \tag{26}$$

Assuming on-resonance excitation, a uniform FA is applied at the time of an assumed infinitesimal RF pulse and relaxation occurs after the RF pulse. Under these assumptions, the FLASH MR signal, *S*, in steady state can be described by the Ernst equation [22]

$$S = A \sin(\alpha) M_{z}^{-} \cdot E_2, \tag{27}$$

where the amplitude of the gradient echo is M_0*A under complete longitudinal relaxation (assuming a $\pi/2$ excitation pulse and TE = 0), and α is the nominal FA. The $\sin(\alpha)$ factor describes the excitation of M^{-}_{xy} and $E_2 = e^{-TE/T_2^*}$ describes the effective transverse relaxation.

Note that the regular Ernst equation in Equation 27 neglects in-pulse relaxation. Thus, to account for in-pulse relaxation effects, to be expected in tissues with short T_2 where the RF pulse cannot be approximated to be infinitesimally short, the Ernst equation has to be modified [15].

[1] The upper indexed plus sign denotes the magnetization after the excitation, whereas the upper indexed minus sign denotes the magnetization before the excitation.

2.4.1 Variable flip angle (VFA) based T_1 measurement

The VFA method is used to calculate T_1 with a significantly shorter acquisition time than for the inversion recovery (IR) technique [20]. The method involves acquisition of FLASH images over a set of FAs. The VFA method can be applied with at least two actual FAs [23]. As a result, a signal curve is generated, which can be rewritten in a linear form, i.e., $y = k \cdot x + m$, as follows [24].

$$\frac{S(\alpha)}{\sin(\alpha)} = E_1 \cdot \frac{S(\alpha)}{\tan(\alpha)} + A \cdot (1 - E_1) \tag{28}$$

Equation 28 assumes constant TR and incremented FA. By using linear regression, the slope, E_1, can be used to determine the apparent T_1:

$$T_1^{app.} = -\frac{TR}{\ln(E_1)} \tag{29}$$

The T_1 values derived using the VFA method can only be regarded as apparent T_1 due to the inhomogeneity in the FA at higher magnetic field strengths [25]. Among others correction methods, a FA map has to be acquired to correct the nominal FAs according to [26].

2.4.2 New approach of linearizing the signal equation

Recently, a new way of linearizing the signal in Equation 27 has been presented [27]. The signal equation with $R_1 = 1/T_1$ can be well approximated by

$$S = A\alpha \frac{R_1 TR}{R_1 TR + \alpha^2/2}, \tag{30}$$

where E_2 is included in A and $\alpha^2/2 \approx 1 - \cos(\alpha)$ represents the PSD. In Equation 30, $R_1TR \ll 1$ and $\alpha \ll 1$. Reduction of PSD by a fraction v, independent of α, is thus implemented as

$$S = A\alpha \frac{R_1 TR}{R_1 TR + (1-\mathrm{v})\alpha^2/2} = A\alpha \frac{R_1 TR/(1-\mathrm{v})}{R_1 TR/(1-\mathrm{v}) + \alpha^2/2} \tag{31}$$

Comparing Equation 30 to the right hand side of Equation 31 shows that a VFA experiment yields an apparent R_1 of $R_1/(1-v)$. Thus, $T_1^{app.} = (1-v)*T_1$, indicating that a reduction of PSD by v appears as a reduction of T_1 by v.

Equation 30 can be rewritten in linear form as

$$\frac{S}{\alpha} R_1 TR + S\alpha/2 = A R_1 TR \tag{32}$$

$$\Leftrightarrow$$

$$\frac{S}{\alpha} = A - S\alpha \frac{T_1}{2TR} \tag{33}$$

A linear regression of Equation 33 directly yields the amplitude as the intercept and T_1 from the slope. The covariance of errors is significantly reduced compared to Equation 28. This novel

approach also has the advantage of being able to show deviations from the signal equation in Equation 27, which are masked when using Equation 28 [28].

A linear plot of the signal data points, collected at different FAs, can be created as $y = S(\tau)/\tau$ over $x = S(\tau)*\tau$, where $\tau = 2*\tan(\alpha/2)$. By introducing this transformation the signal data points that clearly deviate from the linear plot can be excluded.

3. Material and methods

3.1 Simulation of Bloch equations

In order to model the exact behavior of the magnetization during the RF pulse, and thus to obtain the correct magnetization for MW and IE-water, the Bloch equations, i.e., Equation 14, Equation 15 and Equation 16, have to be solved numerically. This was performed by the Runge Kutta^{4th} method using the *ode45* function, with a step width of 0.1 ms, in Matlab 2014b (The MathWorks, Inc., Natick, MA, United States). The in-pulse relaxation processes were considered to occur during the entire RF pulse duration. The initial condition was M_0= [0 0 1]. The T_1 and T_2 values for MW were taken from [29] and [3], respectively. The T_2 for the IE-water was taken from [3] where the T_1 was roughly estimated, as presented in Table 1.

Table 1: Relaxation times, T_1 and T_2, for MW and IE-water.

Type of water	**T_1 [ms]**	**T_2 [ms]**
MW	170	15
IE-water	1000	80

To detect the MW indirectly, the pulse duration was set to 10 ms, which is of the same order as the MW transverse relaxation time. Thus, the T_2 in-pulse relaxation effects can no longer be neglected. The RF pulses used here were truncated SINC with two side lobes, Gaussian and RECT described by Equation 18, Equation 19, and Equation 20, respectively. The used shape parameters were: t_0 = 10 ms /2 = 5 ms for the SINC pulse and σ = 7.434 for the Gaussian pulse.

The transverse and longitudinal magnetizations were studied immediately after different excitation RF pulses, as function of T_2. The T_1 time was set to infinity (i.e., 10^5 s) to only study the transverse relaxation during the RF pulse. The relative difference of the fraction of M^+_z component could not be compared for different FAs. Therefore, it was more suitable to use the PSD in order to study the in-pulse T_2 relaxation impact on the M^+_z component. The Bloch equations were simulated to obtain the PSD for each population (MW and IE-water) using Equation 26. Then, the PSD immediately after the RF excitation pulse, was plotted as a function of the FA from 1° to 90°. This was performed to observe any variation of the relative difference in the PSD between MW and IE-water. To study the excitation profile of the different RF pulses, the magnetizations in x, y and z directions immediately after different RF pulses for the MW and IE-water were simulated and then plotted as a function of the offset frequency, $\Delta f = \Delta\omega/2\pi$.

3.2 Pulse programming

The pulse shape and duration in the standard Siemens FLASH sequence were modified using the sequence development environment, VD13A software, of the *Integrated Development Environment for (MR) Applications* (IDEA, Siemens Healthcare, Erlangen, Germany). This was done in order to experimentally observe in-pulse relaxation effects. Based on the results obtained from the simulations in Matlab, a Hanning-filtered Gaussian pulse of the FLASH sequence was chosen with two pulse durations, 10 ms and 0.5 ms. Furthermore, the number of samples of each pulse was set to 500 for the 10 ms pulse duration and 250 for the 0.5 ms pulse duration.

3.3 Phantoms and MRI unit

Prior to using the modified FLASH sequence in vivo, measurements of relaxation times were performed on three samples of cream with different fat contents (Skånemejerier) and also in the WM and GM of a formalin-fixated pig brain. The relaxation time measurements were performed in order to investigate whether the used phantoms exhibit large in-pulse relaxation effects from the BE simulations, prior the VFA measurements, that can be measured as a reduction of the apparent T_1 when using the long RF pulse.

Table 2: Contents per 100 g for three different cream products according to product label (Skånemejerier, Malmö).

Fat content [%]	**Fat [g]**	**Protein [g]**	**Carbohydrates [g]**
12	12	3.1	4.3
27	27	2.6	3.6
40	40	2.1	3.0

The dairy cream was poured into separate 50 ml vacutainers, and sealed with minimal air bubbles. The cream phantoms were stored in a refrigerator and about 2 h before the experiment the phantoms were placed in room temperature.

All experiments were performed on a 3 T Siemens Magnetom Skyra, and the standard Siemens head/neck RF receiver coil (20-channel matrix coil) was used. The three cream phantoms and the pig brain were placed at the center of the head/neck coil, as shown in Figure 6.

A B

Figure 6: The MR camera setup of A) in vitro experiment and B) ex vivo experiment.

3.4 Experiments

3.4.1 T_1 measurement (in vitro and ex vivo)

The measurements of T_1, for WM and GM in the pig brain, and the T_1 of the water and fat, for the three phantoms, were accomplished using a single slice IR sequence. The parameters used for the ex vivo measurement were: TE = 12 ms, slice thickness = 5 mm, FA = 150°, matrix size = 52 × 128, field of view (FOV) = 60 × 149 mm^2, bandwidth = 130 Hz/pixel, axial orientation, inversion time (TI) = 2900, 2000, 1500, 1000, 700, 500, 400, 250, 150, 100 and 50 ms, and TR = 12900,12000, 11500, 11000, 10700, 10500, 10400, 10250, 10150, 10100 and 10050 ms.

The parameters for the in vitro measurement were the same, except for the use of matrix size = 32 × 128, FOV = 40 × 160 mm^2, an additional TI measuring of 25 ms, and TR = 10030 ms.

3.4.2 T_2 measurement (in vitro and ex vivo)

The measurements of the T_2 values of the pig brain and cream phantoms were performed using a single slice 2D SE sequence. The same orientation, pixel bandwidth and slice thickness as in the T_1 measurement were used. The parameters that differed were, for the ex vivo measurement, matrix size = 63 × 128, FOV = 75 × 150 mm^2, TE = 12, 20, 30, 45, 65, 95, 135 and 200 ms, and TR = 5010, 5010, 5020, 5020, 5030, 5050, 5070, and 5100 ms. The parameters in the in vitro experiment that differed from the ex vivo T_2 measurement were matrix size = 48 × 128, FOV = 45 × 120 mm^2, two additional TEs, i.e., 300 and 450 ms, and thus two TR values, 5150 and 5230 ms.

3.4.3 VFA based T_1 mapping (ex vivo and in vivo)

The investigation of the in-pulse relaxation effects of the pig brain was performed using the modified FLASH sequence with a Gaussian pulse and with 10 ms and 0.5 ms pulse durations. The VFA method was used to create a pixel-by-pixel apparent T_1 map, according to Equation 29. The parameters used for the Gaussian pulse experiment were TR = 16 ms, TE = 8 ms, matrix size = 128 × 88 × 80, FOV = 96 × 140 mm^2, coronal orientation, slice thickness = 2 mm, bandwidth = 500 Hz/pixel and nominal FAs of 5°-41° with a nominal FA increment of 4°.

The VFA based T_1 mapping, in the same manner as described above, was also performed on a 23 year old male volunteer, who had given informed consent. The following parameters were used: TR = 15 ms, TE = 7.38 ms, matrix size = 128 × 124 × 128, FOV = 232 × 240 mm^2, slice thickness = 1.30 mm, bandwidth = 500 Hz/pixel and nominal FAs of 5°-20° with a FA increment of 5°. Furthermore, a 3D magnetization prepared rapid acquisition of gradient echo (MP-RAGE) sequence was used to obtain T_1 weighted images. These images can be used for co-registering of the images obtained from the VFA method, which have lower spatial resolution, to reduce motion artifacts. The following parameters were used for the MP-RAGE sequence: TR = 1900 ms, TE = 2.46 ms, slice thickness = 0.94 mm, matrix size = 248 × 192 × 256, FOV = 232 × 240 mm^2, FA = 9° and bandwidth = 180 Hz/pixel.

3.4.4 Phase images (ex vivo and in vivo)

A map of the B_0-field inhomogeneity in the sample was obtained by acquiring phase images using a two-echo 2D GRE sequence. The following parameters were used for the ex vivo subject: Matrix size = 80x128, FA = 70°, slice thickness = 2 mm, ΔTE = 2.46 ms, TR = 420 ms, bandwidth = 500 Hz/pixel and FOV = 84 × 140 mm^2. For the in vivo test person, the parameters that differed from the ex vivo case as follows: Matrix size = 84 × 100 and FOV = 168 × 140 mm^2.

3.5 Data analysis

3.5.1 Post-processing of relaxation times data (in vitro and ex vivo)

For each obtained image from the in vitro and ex vivo relaxation times measurements, an elliptical region-of-interest (ROI) was drawn within the WM and GM of the pig brain, and within each of the cream phantoms, respectively, and then, the mean signal of the drawn ROI was recorded. The ROI placement using RadiAnt DICOM Viewer, version: 1.9.16.7446, for both the ex vivo and the in vitro measurements, are shown in Figure 7.

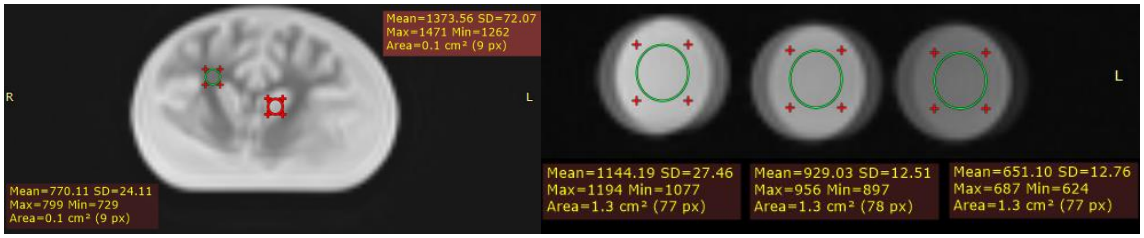

A B

Figure 7: Coronal MR images showing ROI placement within A) the GM (red ellipse) and WM (green ellipse) of the pig brain, and B) the three cream phantoms. Note the chemical shift artifacts in the cream phantoms.

The obtained data points from the T_1 measurement were plotted as a function of the TI. The obtained data points from the T_2 measurement were plotted as a function of TE. A mono-exponential function was non-linear least-squares fitted to the obtained T_1 and T_2 signal data of the ex vivo measurement. The cream phantoms consist of water and fat, and thus a bi-exponential model was fitted, in a least square sense, to the data points. This was performed by fitting the corresponding amplitudes, for water and fat, and relaxation times, i.e., $T_{1,water}$, $T_{1,fat}$ and $T_{2,water}$, $T_{2,fat}$, respectively. The uncertainty in the fitted parameters was obtained by an approach to bootstrapping, as explained below.

In order to determine whether the cream phantoms were expected to exhibit any in-pulse relaxation effects, the relaxation times obtained for the water and fat in the 12 % cream phantom were used in the simulation of Bloch equations as explained in Section 3.1. The reason for choosing the 12 % cream phantom was that is showed less uncertainties compared with the other cream phantoms.

Estimation of the uncertainty in the fitted parameters

In order to estimate the uncertainty of the fitted parameters, an approach to bootstrapping in regression problems was performed by estimating the population distribution using the information based on a number of randomly resamples. The parameters were fit nonlinearly, and thereby the residuals were calculated for each of the data points. The obtained residuals were then resampled with replacement from the sample, meaning that a new set of randomly resampled residuals were generated. The new residuals were then added to the predicted model values at each TE, which led to a new bootstrapped data set. The model was fitted again, which generated another set of model parameter estimates. This procedure was repeated 500 times, which gave a distribution of estimated parameters. By calculating the standard deviation of the obtained distribution, the uncertainty of the fitted parameters to the signal equation model was obtained.

3.5.2 Post-processing of VFA method data (ex vivo and in vivo)

The measured data obtained from the VFA method at different FAs were analyzed by creating a linear plot using the transformation described in the theory section. This was done in order to exclude signal data points that clearly deviated from the linear plot. In order to obtain this linear plot, the acquired signals for the ex vivo and in vivo data were obtained drawing a ROI within each test subject. This was accomplished using the locally developed software Eval Gui

(Markus Nilsson, Lund University, Lund, Sweden). The ROI placement within each of the test objects is shown in Figure 8.

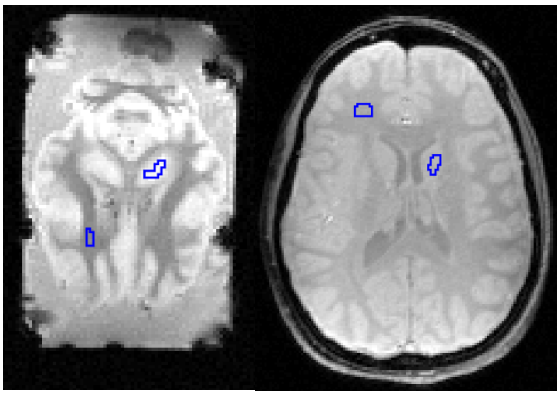

A B

Figure 8: ROI placement within the WM (low signal) and GM (high signal) for A) the pig brain and (B) the brain of a healthy volunteer. The two brains are not to scale.

In order to create parametric maps of results for the two used pulse durations, the apparent T_1 was first obtained pixel-by-pixel using Equation 29 instead of Equation 33 for simplicity and easier handling of the apparent T_1 calculation. A relative difference between the two obtained apparent T_1 maps, with different pulse durations, was then calculated as

$$\frac{T_{1,0.5ms}^{app.} - T_{1,10ms}^{app.}}{T_{1,0.5ms}^{app.}} \tag{34}$$

The pixel-by-pixel apparent T_1 maps of the healthy test person were co-registered with the 3D MP-RAGE images, which served as reference, using *FMRIBs Linear Image Registration (FLIRT)* tool. This tool performs a rigid body transformation of the image volume. This was performed by image interpolation to obtain better spatial resolution, but also to reduce the motion between images.

4. Results

4.1 The T_2 dependence of M^+_{xy} and M^+_z

The transverse and longitudinal magnetizations M^+_{xy} and M^+_z respectively, after excitation by the RECT, Gaussian and SINC pulses with FA = 30°, were studied with respect to the dependence of T_2 relaxation times during the nutation.

For a T_2 range between 1 ms and 10 s, the simulated M^+_{xy} component was compared to a reference curve, ref $(M^+_{xy}) = \sin(\pi/6)\cdot e^{-(0.5\cdot T_{RF}/T_2)}$, that assumes T_2 relaxation after instantaneously created M^+_{xy} at a half of the actual RF pulse duration (Figure 9 A). The curves are nearly identical except for $T_2 < 10$ ms. Equal curves indicate that a modification of the signal equation in Equation 27 is not required. This is more clearly seen by the relative difference from the reference curve, $ref(M^+_{xy}) - M^+_{xy} / ref(M^+_{xy})$, as shown in Figure 9 B. The T_1 relaxation time was assumed to be infinite during the RF pulse duration.

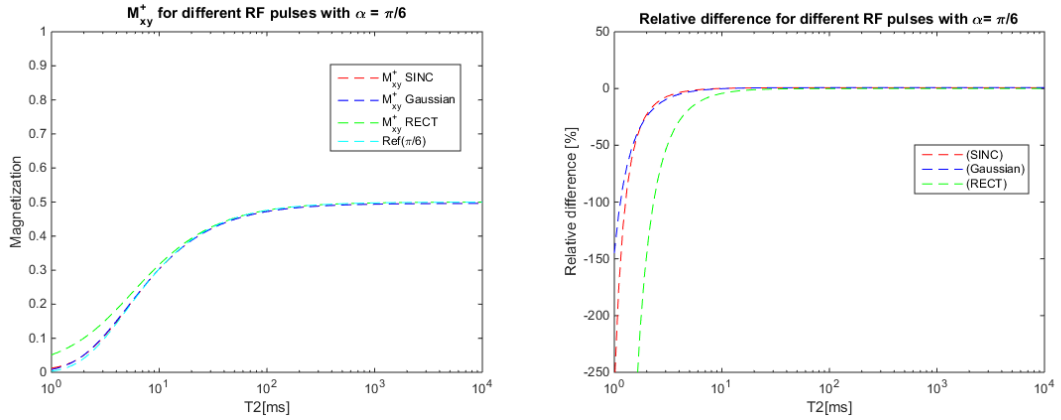

A B

Figure 9: A) The transverse magnetization, M^+_{xy} as a function of T_2, immediately after irradiating with different RF pulse shapes with T_{RF} =10 ms and FA=30°, and a reference curve representing relaxation occurring after an instantaneous RF pulse located at half of the actual pulse length. B) The relative difference of obtained M^+_{xy} from the reference curve for different RF pulses. The T_1 is set to 10^5 s.

In Figure 10, the M^+_z component was compared to the reference (black solid line) given by the signal equation in Equation 27, ref $(M^+_z) = \cos(\pi/6)$). This assumes that the M^+_z component is independent of in-pulse T_2 relaxation as in the conventional signal equation in Equation 27, as shown in Figure 10 A. The relative difference from the reference curve, $(1 - ref(M^+_z) - (1 - M^+_z)/1 - ref(M^+_z)$, is shown in Figure 10 B.

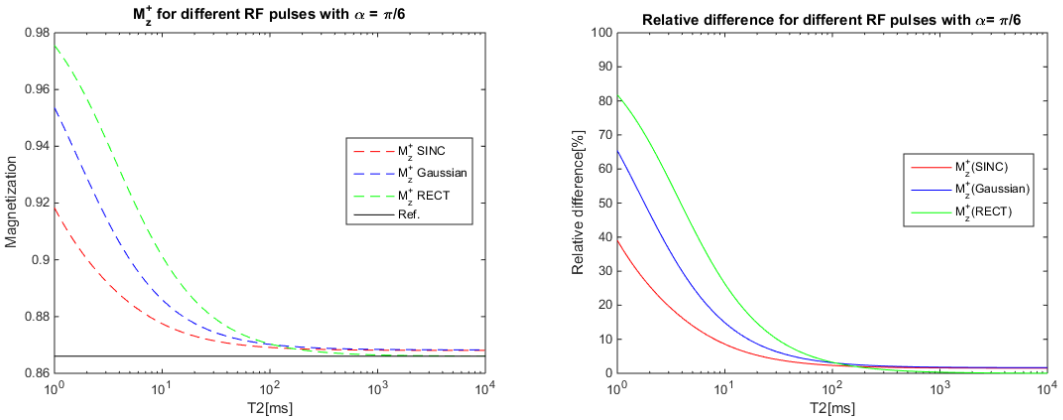

A B

Figure 10: A) The longitudinal magnetization, M^+_z, as a function of T_2, immediately after irradiating with FA = 30° using different RF pulses, and a reference line representing an independent longitudinal magnetization of T_2. B) The relative difference of the obtained M^+_z from the reference curve for different RF pulses. The T_1 is set to 10^5 s.

The curves corresponding to the Gaussian and SINC pulses in Figure 10, do not converge to the reference line. A programming error, such as long step length or incorrect calculation of the area under the RF pulse which leads to a lower FA, could have caused this offset, but the reason is not clearly understood.

The simulated M^+_z curves and the reference line are not in agreement in the 1-100 ms T_2 region. This can be explained by the in-pulse T_2 relaxation that affects the M^+_z when using a long RF pulse, i.e., 10 ms, and thus the signal equation in Equation 27 has to be modified in order to take into account the in-pulse T_2 relaxation effect on M^+_z.

4.2 PSD for MW and IE-water

In Figure 11 A and B, the PSDs for different RF pulses are shown, i.e., RECT, Gaussian and SINC, with T_{RF} = 10 ms as a function of the FA. This was performed in order to show which pulse shape gave the largest relative difference between the MW and IE-water. For clarity, the relative difference between the PSDs of the two populations was plotted as a function of the FA, shown in Figure 11 C.

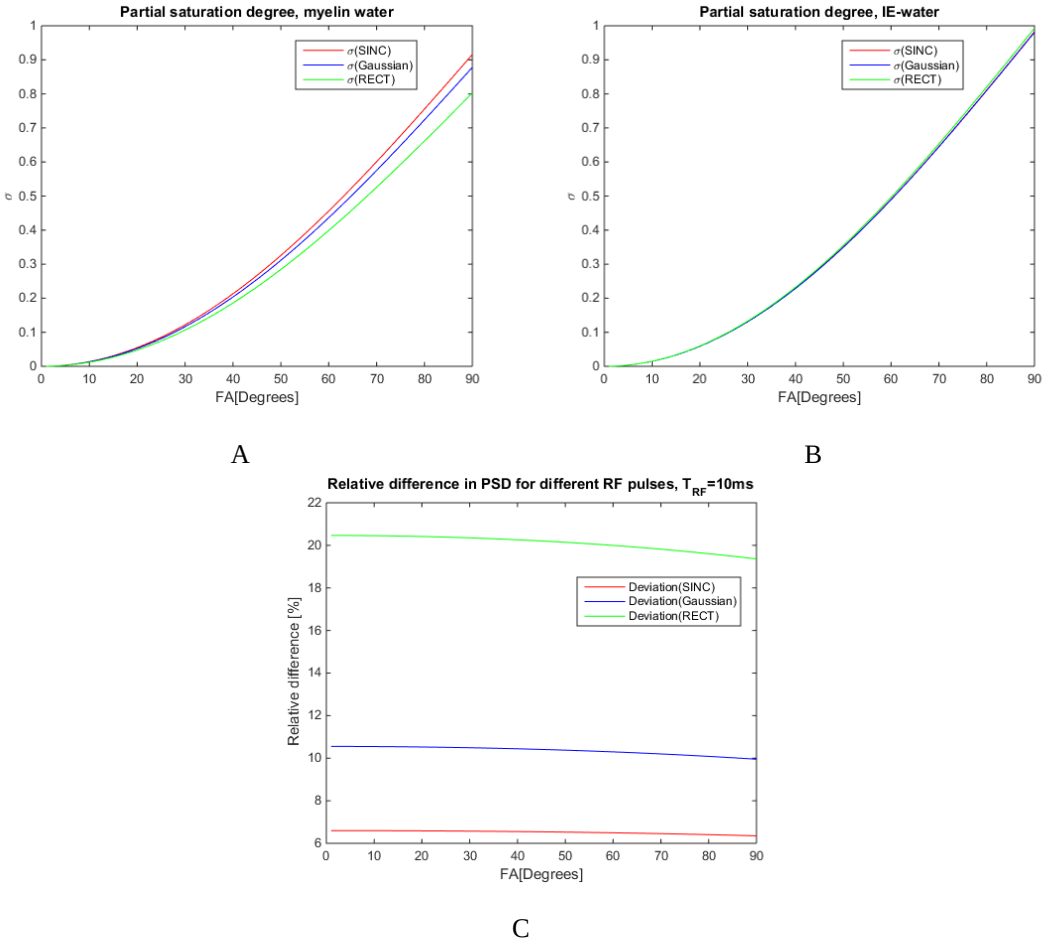

Figure 11: PSD (σ) immediately after different RF pulses as a function of FA, simulated for A) the MW and B) IE-water. The relative difference of the PSD between the MW and IE-water is shown in C. The pulse length used here was T_{RF}= 10 ms.

Observed in Figure 11 A and B is that the PSD is dependent on the FA. According to Figure 11C, there is some variation of the relative difference over the whole FA range, but it is almost constant for FA < 30° .The RF pulse that imposes the largest effect of in-pulse T_2 relaxation on M_z^- is the RECT pulse. The SINC gave smallest effects, and the Gaussian pulse was an intermediate case.

4.3 Excitation profile

The simulated magnetizations in x, y and z direction for the MW and IE-water were studied as a function of the offset frequency, Δf, to study the excitation profiles for the different RF pulses. This was performed in order to determine which of the three RF pulses that provide an excitation profile with least degradations in the M_y^+ component to avoid a potentially bias and increased variance in the apparent T_1. The results are shown in Figure 12, where the simulated magnetization is observed immediately after irradiating with different RF pulses with T_{RF} = 10 ms and FA = 30°.

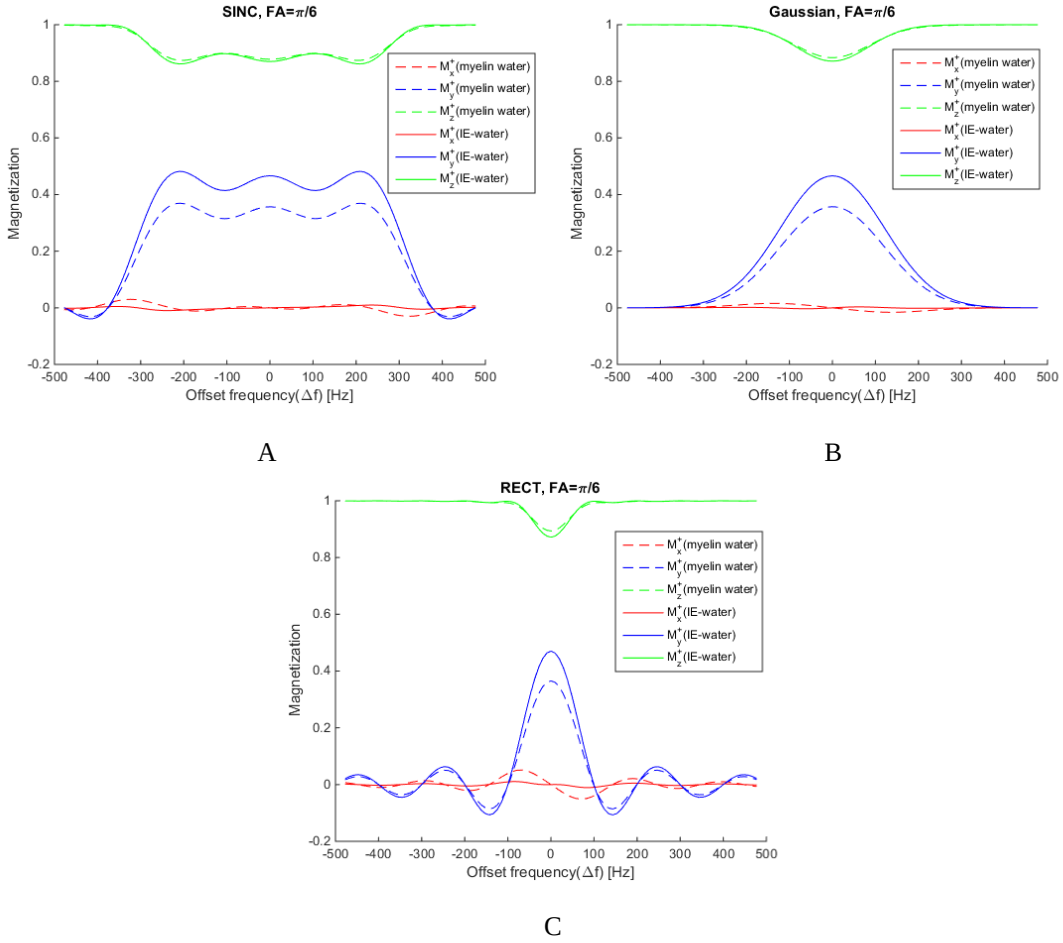

Figure 12: The magnetizations in x, y and z directions for MW and IE-water as a function of the offset frequency, Δf, immediately after A) a truncated SINC, B) Gaussian and C) a RECT pulse with FA = 30°. The pulse length used here was T_{RF}= 10 ms.

The visual inspection results for Δf = ±500 Hz, lead to the conclusion that the RECT pulse returned the smallest full width at half maximum (FWHM) of the M^{+}_{y} component. In addition, the RECT pulse gives most modulation of the M^{+}_{x}, leading to a non-zero M^{+}_{x} component. Hence, the RECT pulse gives most degradation in the M^{+}_{y} component while the SINC pulse gives the least amount of such effects. Furthermore, the reduction of the M^{-}_{z} component is due to the created M^{+}_{x} and M^{+}_{y} components, which generates additional partial saturation.

4.4 Relaxation times measurement (in vitro)

For the three cream phantoms, the fitted T_1 and T_2 signal curves in Figure 13 and the fitted T_1 and T_2 values in Table 3 were obtained when fitting a bi-exponential model to the acquired data.

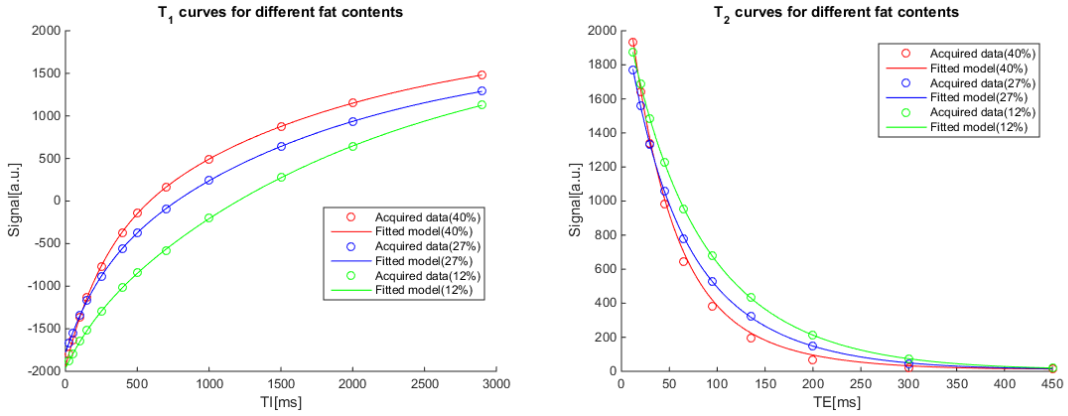

A B

Figure 13: A) T_1 signal curves and B) T_2 signal curves for the 12 %, 27 % and 40 % cream phantoms.

Table 3: Measured relaxation times for the 12 %, 27 % and 40 % cream phantoms and their uncertainty.

Fat content [%]	**$T_{1,water}$ [ms]**	**$T_{1,fat}$ [ms]**	**$T_{2,water}$ [ms]**	**$T_{2,fat}$ [ms]**
12	2007.7±59.0	204.5±19.1	94.3±2.0	37.1±4.0
27	1699.6±47.6	236.0±9.0	90.7±6.0	37.4±4.7
40	1770.1±102.2	256.9±10.2	94.9±41.5	38.5±6.0

Simulated data of difference in PSD between fat and water (Figure 14) were obtained using the relaxation times measured on the 12 % cream phantom in Table 3. The relative difference between the PSDs of the two populations, i.e., fat and water, was plotted as a function of the FA. Figure 14 shows reduction of roughly half of the relative difference between the PSD of the water and fat compared with the results obtained for the MW and IE-water. The same impact of the pulse shapes on the PSD as seen in Figure 11 C is observed in Figure 14.

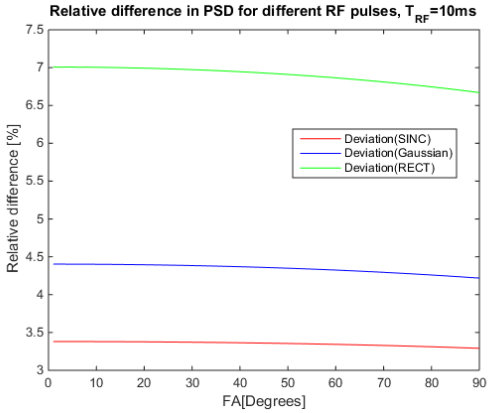

Figure 14: The simulated relative difference of the PSD between the fat and water in cream with the relaxation times of the 12 % cream phantom in Table 3 The pulse length used here is T_{RF}= 10 ms.

4.5 Relaxation times measurements (ex vivo)

For the fixated pig brain, the fitted T_1 and T_2 signal curves in Figure 15 and the fitted T_1 and T_2 values in Table 4 were obtained by fitting a mono-exponential model to the mean signal of a ROI, because the signal from MW and IE-water could not be separated.

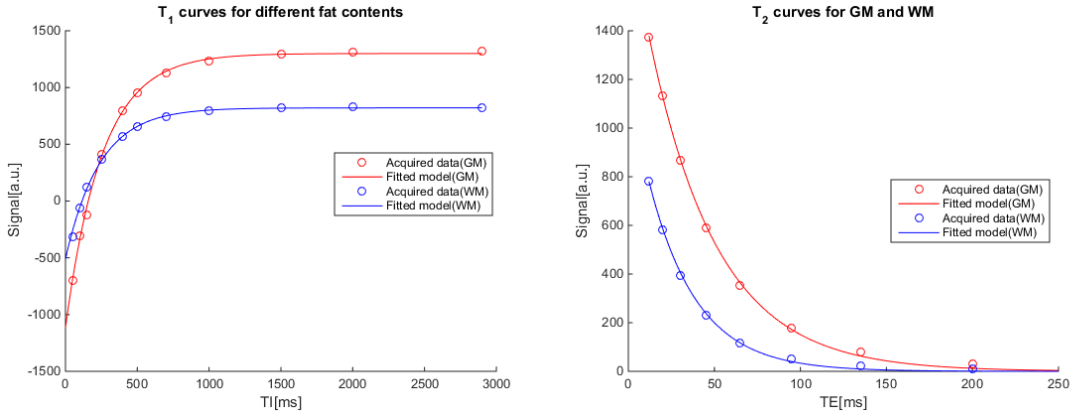

A B

Figure 15: A) T_1 signal curves and B) T_2 signal curves for GM and WM in the pig brain.

Table 4: Measured relaxation times and their uncertainty for the pig brain.

Tissue	**T_1 [ms]**	**T_2 [ms]**
GM	255.9±7.2	39.8 ±0.50
WM	238.2±7.3	27.9±0.58

4.6 Linear plot of the VFA FLASH signal (ex vivo and in vivo)

For preliminary tests of VFA data quality, ROIs were placed in GM and WM of one slice. Figure 16 shows $y = S(\tau)/\tau$, obtained using the Gaussian pulse for the ex vivo and in vivo measurements, plotted as a function of $x = S(\tau)*\tau$. Deviations from the linear plots in the graphs below were observed for nominal FAs higher than 29° for the ex vivo measurement (not shown in Figure 16). These images were thus excluded in calculations of the apparent T_1.

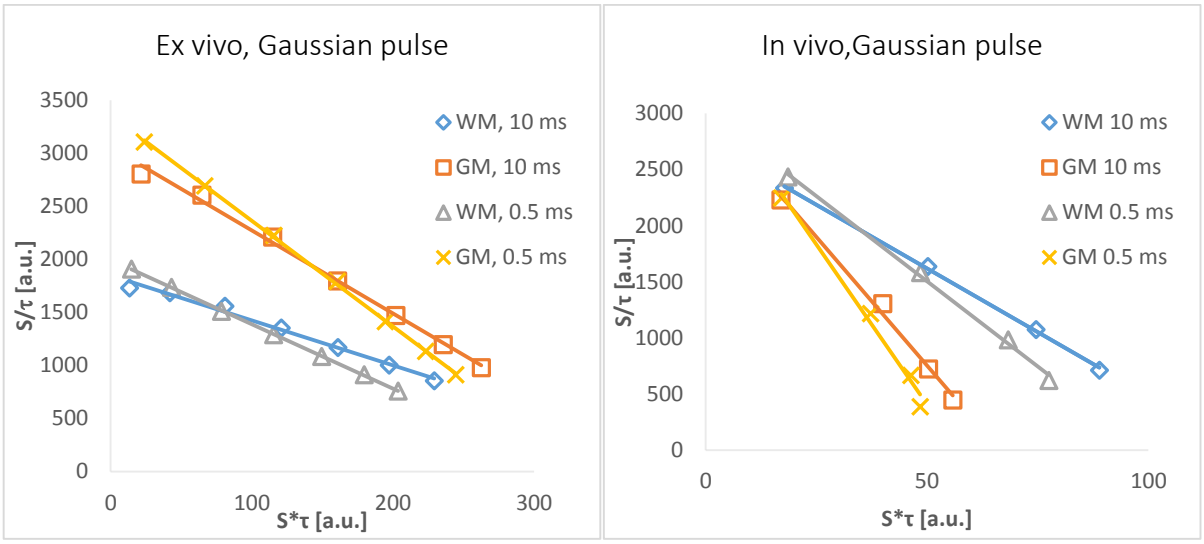

A B

Figure 16: Linear plots of the S/τ as a function of S*τ, using a Gaussian pulse for A) the ex vivo measurements and B) in vivo measurements. Steeper slope indicates higher apparent T_1 values.

According to Figure 16, the linear plots of the WM and GM data using a 0.5 ms pulse exhibit steeper slopes in both the ex vivo and in vivo measurements than in the corresponding linear plots of the WM and GM using a 10 ms pulse. This indicates higher apparent T_1 values for the 0.5 ms pulse than the 10 ms pulse.

4.7 Apparent T_1 maps (ex vivo and in vivo)

Figure 17 shows pixel-by-pixel apparent T_1 maps of the pig brain using Gaussian pulses, with 0.5 ms and 10 ms pulse durations. It also shows the relative difference between the two maps obtained for different pulse durations, as explained in the methods section.

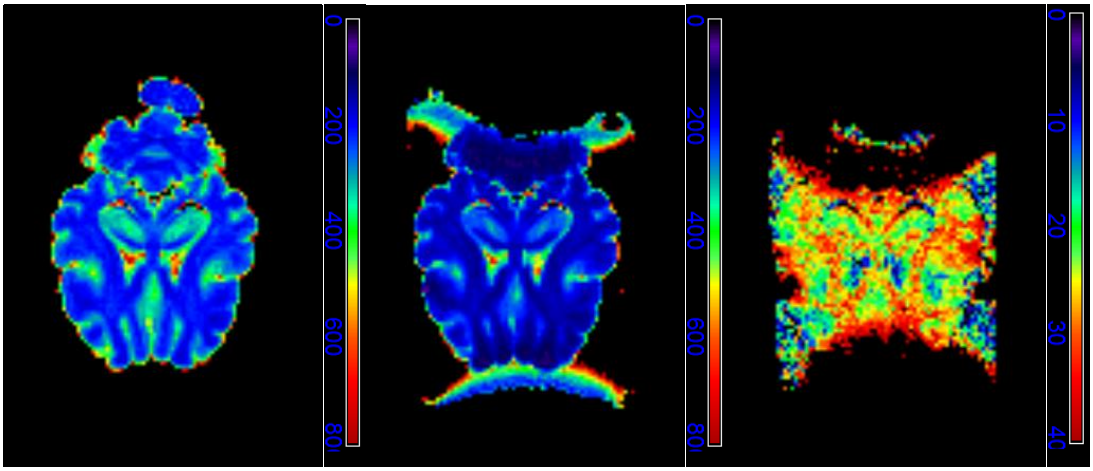

A B C

Figure 17: Axial center slice of an apparent T_1 map of the pig brain for A) 0.5 ms and B) 10 ms Gaussian pulse durations. The relative difference between the two apparent T_1 maps is shown in C).

The GM exhibited higher apparent T_1 values than the WM. Signal loss caused by inhomogeneities in B_0 can be observed close to the upper and lower edges of the object in Figure 17 B. This leads to about 100 % relative difference between the two apparent T_1 maps. However, higher than expected relative difference, i.e., about 30 %, is observed in the WM.

Figure 18 shows a phase image of the pig brain, and also a histogram that shows the number of voxels with different voxel phase values. The B_0-field is homogenous (i.e., frequency offset close to zero) only in a small region in the center of the object, leading to a large spread of voxel values in the histogram.

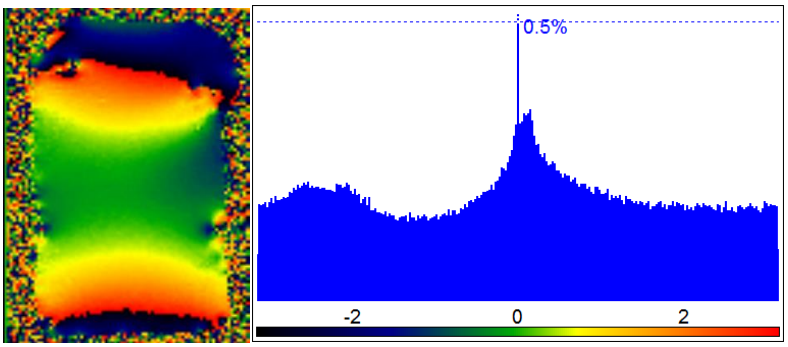

A B

Figure 18: A) Axial center slice of phase map of the pig brain. B) Histogram showing the phase of the voxels in radians. Note phase aliasing from π to $-\pi$ close to edges of sample in the image.

The apparent T_1 maps of a healthy test person, using a Gaussian pulse with 0.5 ms and 10 ms durations, were co-registered with a 3D MP-RAGE sequence to obtain better spatial resolution, but also to reduce motion artifacts. Figure 19 shows the co-registered apparent T_1 maps and also the relative difference in apparent T_1 between the long pulse and the short pulse, as explained in the methods section.

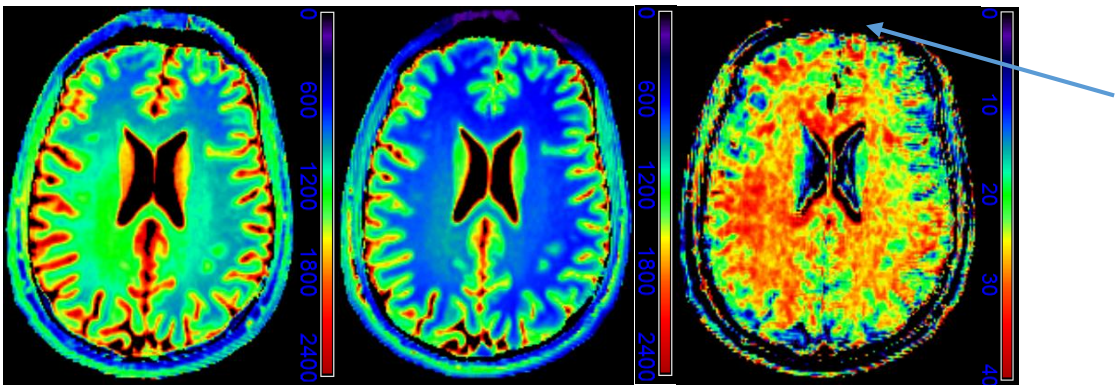

A B C

Figure 19: Axial center slice of apparent T_1 maps of a healthy volunteer, obtained after co-registration with a 3D MP-RAGE sequence, for A) 0.5 ms and B) and 10 ms Gaussian pulse durations. The relative difference between the two apparent T_1 maps is shown in C).

Effects of B_0-inhomogeneities were observed just outside the brain in Figure 19 B. This leads to a high relative difference in this location (blue arrow) as seen in Figure 19 C. This was confirmed in Figure 20, i.e., large phase change just outside the brain. Figure 20 shows a phase image of a human brain, and also a histogram showing the number of voxels with different voxel phase values. The B_0-field was relatively homogenous in large regions of the object,

which is consistent with the fact that the most voxels values are gathered close to the center of the histogram.

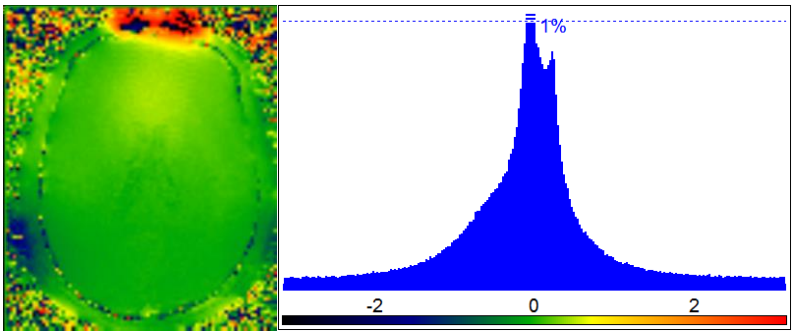

A B

Figure 20: A) Axial center slice phase map of a healthy volunteer. B) Histogram showing the phase of the voxels in radians. Note better B_0 homogeneity than in Figure 18 A.

The comparison between Figure 17 A and B leads to the conclusion that when using the long RF pulse the apparent T_1 values are reduced. The same observation can be made in Figure 19 A and B.

5. Discussion

In this work, the effects of in-pulse T_2 relaxation during the RF pulse was studied in FLASH MRI, and the specific question to be addressed was whether it is feasible to exploit these effects to selectively detect MW in the human brain. The proposed approach exploits the fact that the MW, which constitutes about 15 % of the water signal in myelinated WM [3], shows distinctly shortened T_2 time than IE-water. The present study was a feasibility study, and, according to the best of our knowledge, there is no previous literature on this topic.

Comparing the method evaluated in this study with the existing myelin-sensitive MRI techniques [30], there are some potential advantages with the presented study in terms of easily clinical implementation and more reliability assuming that the MT effects can be separated from the in-pulse relaxation effects. The MWF technique presented in [30] has, among other, challenges such as finding the algorithm in extracting the myelin water signal from T_2 decay curves and also developing the model for interpretation of the T_2 decay curve [2]. A disadvantage with the MWF technique is the decreased MWF that can be caused by edema or inflammation, and the method is not specific measure of myelination [14]. This disadvantage can also be true for the proposed method, i.e., reduction of apparent T_1 in WM is not necessary due to demyelination of the axons. However, the presented study in this thesis provides a basis for MRI based future studies aimed to diagnostic patients with demyelinating disorders, e.g. MS.

5.1 Simulation of Bloch equations

The purpose of the simulations in Matlab, prior to the pulse programming, was to find an RF-pulse shape that imposes a different degree of partial saturation, see Equation 26, on MW by in-pulse transverse relaxation effects during a long RF pulse of 10 ms. This partial saturation, leads to a change in the apparent T_1 map when compared to the short (0.5 ms) RF pulse. Generally, the longitudinal relaxation time was expected to be long compared to the RF pulse length, and therefore neglected. Another purpose was to understand the dynamic behavior of the magnetization during different RF pulses, and also to investigate off-resonance effects for different RF pulses.

The conclusion from Figure 9 is that the conventional approximation of the M_{xy}^{+} component, i.e., that it is created instantaneously at the center of the actual RF pulse and then subject to relaxation, is consistent with the simulations (including relaxation during the entire RF pulse), but only if T_2 is longer than the pulse length. This finding was observed for the RECT pulse bur for the Gaussian and SINC pulses, the conventional approach and the simulations are consistent for $T_2 \geq 2$ ms, i.e., even shorter than the pulse length. Hence, for T_2 shorter than the pulse length, i.e. $T_2 \leq 2$ ms, results from these two approaches deviate, which is relevant, for example, UTE measurements [22]. Figure 10 explains that the conventional view on M_z^+, i.e., being independent of T_2, and the proposed approach, where M_z^+ depends on T_2, are inconsistent with each other for T_2 values less than 100 ms. Thus, this disagreement between the two approaches allows us to separate the MW and IE-water because they result in different PSDs.

The RF pulse length was chosen to be of the order of the transverse relaxation time of MW. The shape of RF pulse also influences the in-pulse relaxation effects, since $\omega_1(t)$ determines the temporal behavior of the magnetization vector during the RF pulse. The RECT pulse is applied

constantly over the entire duration, see Figure 2. For example, some transverse magnetization is generated early and is thus subject to transverse relaxation effects during a long time. This may explain why the RECT showed the largest difference of M^{+}_{xy} from $\sin(\alpha) \cdot e^{-(0.5 \cdot T_{RF} / T_2)}$ and also the largest reduction in PSD. In the early and late periods of a Gaussian pulse, the nutation is slow and the main flip motion occurs during the middle period of the pulse. This may explain why less in-pulse transverse relaxation effects are seen, compared to the RECT. The main flip motion of a SINC is even more compressed around the center than for the Gaussian, and thus even less transverse in-pulse relaxation effects are observed, and this implies that the least degree of PSD reduction is observed for the SINC. The reason that the pulse shape does not seem to matter when looking at the IE-water is that the T_2 relaxation time is much longer than for MW; no in-pulse relaxation effects are expected because the RF pulse duration is "too short" for them to develop. Furthermore, the relative difference between the PSDs of the two populations is mostly independent of the FA (1°-90°). This is desired when performing VFA measurement and in the presence of FA inhomogeneities, especially at a higher field strength of 3 T [26].

As mentioned above, more in-pulse transverse relaxation leads to less saturation created by a single RF pulse. In the context of a FLASH sequence with $TR << T_1$, this leads to a higher steady state M_z, which in the absence of other explanations, would be interpreted as faster T_1 relaxation.

The Gaussian pulse gives less degradation in the signal intensities than the RECT, and much less such degradations are obtained with the SINC. Therefore, the choice of the SINC pulse would imply lowest in-pulse relaxation effects but greatest robustness with regard to excitation profile. The Gaussian pulse is a compromise between optimal relative difference in PSD between the two populations and optimal excitation profile.

5.2 In vitro study

In order to study an object similar to WM, with its MW and IE-water components, three cream phantoms with different fat contents were investigated. Contrary to WM, the components in cream can be well separated by means of relaxation, but the fat exhibits a frequency offset of about 3.4 ppm, corresponding to 413 Hz at the 2.89 T magnetic field of the MR scanner. To reduce offset effects, the SINC had to be used, with the RF carrier frequency set between the water and fat resonances.

According to Table 2, the 12 % cream phantom should show the lowest total signal from the T_1 measurement, obtained by means of IR. This is because of the large amount of water, which makes the M_z regrowth slower, i.e., T_1 is longer, and thus the M_{xy} becomes smaller after next flipping, implying lower signal. Thus, the higher the fat content is, the higher the total T_1 becomes, because the fat has shorter T_1. This observation is in agreement with the T_1 curves in Figure 13 A. Furthermore, the total signal from the T_2 measurements for the 12 % cream phantom should be highest because it contains most water, and thus longer transverse relaxation time, indicating a slower dephasing of the spins in the M_{xy} plane. This observation is in agreement with the T_2 curves in Figure 13 B. On the other hand, the separated T_1/T_2 values, i.e., $T_{1,2,water}$ and $T_{1,2,fat,}$ should be the same for different fat contents should, because the intrinsic material properties are assumed to be unchanged, and this is approximately what was observed in this study (Table 3). The reason why the fitted $T_{2,water}$ value for the

40 % cream phantom in Table 3 showed a large uncertainty could be that the signal model did not fit into the acquired data very well, as can be observed in Figure 13 B.

The fitted relaxation times, i.e., $T_{2,water}$ and $T_{2,fat}$, for the cream phantoms were found to be higher than the MW and IE-water transverse relaxation times, which is consistent with previous studies [17]. Hence, less pronounced in-pulse relaxation effects can be expected for cream than for MW and IE-water. Therefore a new set of simulations was performed with the relaxation times obtained for the 12 % cream phantom in order to determine the PSD. This enabled determination of the relative difference between the PSDs for the water and the fat. According to Figure 14, the expected relative difference between the water and fat PSDs was about half of the corresponding levels for MW and IE-water in Figure 11. This can be explained by the relatively long relaxation times for the cream phantoms compared with MW and IE-water. A compensation for this could be to double the pulse duration, i.e., to 20 ms, in order to observe in-pulse relaxation effects, but this is an issue because of the loss of signal. However, no VFA measurement was performed in order to verify the simulations due to the relatively small in-pulse relaxation effects observed.

5.3 Ex vivo and in vivo studies

The FLASH signal equation in Equation 29, which was used to estimate the apparent T_1 maps for the long and short RF pulses, should be modified to account for in-pulse relaxation effects observed with the long RF pulse. However, simply mapping the relative difference in apparent T_1 maps between the two pulses will reveal where the difference is largest, i.e., where the transverse relaxation times are of the same order as the long RF pulse duration, and thus where most myelin is likely to reside.

No correction of the FA was performed, and hence B_1-inhomogeneities are likely to exist at the 3 T field strength [26]. This leads, depending on the coil construction, to higher FA in the center of the object and lower FA closer to the edges. The B_1-inhomogeneities are observed in the apparent T_1 maps for the two pulse durations. Fortunately, this effect vanishes when calculating the relative difference between the two apparent T_1 maps in Figure 17 C and Figure 19.

Springer et al. (2010) showed that the in-pulse relaxation effects in UTE measurements in vitro led to a reduction in the apparent T_1 values. Although this case is far more complex than our measurements, the same observation was made in this study. However, the shortening was much stronger than expected from the simulations and considerable shortening was found in GM, where there is hardly any MW [3]. One explanation to this observation may be that, in general and also in this study, the effects of MT are neglected in the signal equation in Equation 27. Unlike MW or IE-water, the magnetization of bound water does not show a nutation, since the transverse magnetization relaxes almost instantly ($T_2 \approx 0.01$ ms). The longitudinal magnetization is decreased by the square of $B_1(t)$ with a very broad absorption line shape. Hence, a partial saturation of the bound pool is caused by the RF pulse, and the MT effects from the partial saturation of the bound proton pool are thus decreasing. Also, the transferred saturation is roughly proportional to the integrated power of the RF pulse, i.e., to α^2/T_{RF} [29]. The shorter the RF pulse, the more MT effects are to be observed [31]. This additional saturation due to MT contributions can be incorporated into the approximated FLASH signal equation in Equation 30 by an additional term in the denominator, δ, which describes the magnetization loss by a fraction *m* due to MT effects [32]. For the short pulse, $\delta = m\ \alpha^2/T_{RF}$.

$$S = A\alpha \frac{R_1 TR}{R_1 TR + \alpha^2/2 + m\alpha^2/T_{RF}} = A\alpha \frac{R_1 TR/(1 + m/T_{RF})}{R_1 TR/(1 + m/T_{RF}) + \alpha^2/2} \quad (35)$$

When neglecting the relaxation effects in the short pulse, we get $T_{1,short} = (1+2m)*T_1$. When neglecting the MT effects for the long pulse, we get $T_{1,long} = (1-v)*T_1$. The relative difference between the two apparent T_1 maps is given by

$$1 - \frac{T_{1.long}}{T_{1,short}} = 1 - \frac{1-v}{1 + \frac{2m}{T_{RF,short}}} \approx v + \frac{2m}{T_{RF,short}} \quad (36)$$

Hence, it can be qualitatively shown that the effect of MT on T_1 enhances that of the in-pulse relaxation. However, the MT effects are likely to have contributed to the observed high relative difference in Figure 17 C and Figure 19 C, while the in-pulse relaxation effects are assumed to be much smaller, i.e., about 10 % for the MW and IE-water in vivo using a Gaussian pulse, according to Figure 11. The relative difference in the WM for the fixated brain and in vivo, i.e., Figure 17 C and Figure 19 C, respectively, is in the same order. The visual comparison between the same figures indicates also that the relative difference is in the same order for the GM. The reason for this may be that the MT effects mask or suppress the relaxation effects, but otherwise the relaxation effects are expected to be more pronounced for the ex vivo subject, due to the relatively short relaxation times in the pig brain compared with the in vivo relaxation times [33]. To summarize, further studies are required in order to elucidate the relative contributions of the MT and in-pulse relaxation effects, and such studies can be performed by varying the pulse duration.

5.3 Study limitations

At filed strengths > 1.5 T, the T_1 quantification using the VFA method is not accurate due to inhomogeneities in the transmit field (B_1^+), which in turn lead to inhomogeneities in the FA [26]. Thus, a limitation of the presented study was that no mapping of the actual FA was performed. This mapping is required in order to determine the relaxation effects, i.e., reduction of T_1 when using the long RF pulse, accurately.

Some error sources could have affected the result from the ex vivo and in vivo measurements. Firstly, some B_0–inhomogeneities were observed in the in vivo measurement, but more pronounced in the ex vivo measurement, and this is confirmed in Figure 20 and Figure 18. Thus, it is difficult to obtain an accurate T_1 map, which is a disadvantage of using this phantom, despite the observed high relative difference in Figure 19 C. Furthermore, the employed relaxation times for the MW and IE-water are not exactly determined [29, 3]. This leads to uncertainties in the expected in-pulse relaxation effects that influence the relative difference between the apparent T_1 maps in the in vivo measurement.

6. Conclusions

Simulations using the Bloch equations for RECT, Gaussian and SINC RF pulses showed that substantial in-pulse relaxation effects for in vivo MW can be created at a pulse duration of 10 ms. The partial saturation of the longitudinal magnetization was found to be reduced by 21%, 11% and 7%, respectively. These values were almost independent of FA, so they can be observed as a reduction of the apparent T_1 obtained by the VFA method using FLASH MRI. In vivo, the map of apparent T_1 reduction showed more reduction in WM than in GM, where there is hardly any MW. However, much larger reductions than expected from simulations, especially in GM, indicated that MT effects in the short RF pulses, not present in the long pulses, may play a major role for this finding. Further studies are required to separate the MT and the in-pulse relaxation effects by variation of the RF pulse duration.

7. References

1. Edelstein W.A., Glover G.H., Hardy C.J. and Redington R.W. *The intrinsic signal-to-noise ratio in NMR imaging.* Magn Reson Med, 1986. **3**(4): p. 604-18.
2. Laule C., Vavasour I.M., Kolind S.H., Li D.K.B., Traboulsee T.L., Moore G.R.W. and MacKay A.L., *Magnetic resonance imaging of myelin.* Neurotherapeutics, 2007. **4**(3): p. 460-84.
3. MacKay A., Whittall K., Adler J., Li D.K.B., Paty D.W. and Graeb D.A., *In vivo visualization of myelin water in brain by magnetic resonance.* Magn Reson Med, 1994. **31(**6): p. 673-7.
4. Gillies Robert J. *NMR in physiology and biomedicine*. 1994, Academic Press, Inc.
5. Deoni S. C.L., Rutt B. K., Arun T., Pierpaoli C. and Jones D. K., *Gleaning multicomponent T1 and T2 information from steady-state imaging data.* Magn Reson Med, 2008. **60**(6): p. 1372-87.
6. Keegan B.M. and Noseworthy J.H., *Multiple sclerosis.* Annu Rev Med, 2002. **53**: p. 285-302.
7. Stewart W. A., MacKay A., Whittall, K. P., Moore, G. R. and Paty, D. W., *Spin-spin relaxation in experimental allergic encephalomyelitis. Analysis of CPMG data using a non-linear least squares method and linear inverse theory.* Magn Reson Med, 1993. **29**(6): p. 767-75.
8. Waldman A., Rees J.H., Brock C.S., Robson M.D., Gatehouse, P.D. and Bydder G.M., *MRI of the brain with ultra-short echo-time pulse sequences.* Neuroradiology, 2003. **45**(12): p. 887-92.
9. Barkovich A.J., *Magnetic resonance techniques in the assessment of myelin and myelination.* J Inherit Metab Dis, 2005. **28**(3): p. 311-43.
10. Song S.K., Sun S.W., Ramsbottom M.J., Chang C., Russel J. and Cross A.H., *Dysmyelination revealed through MRI as increased radial (but unchanged axial) diffusion of water.* Neuroimage, 2002. **17**(3): p. 1429-36.
11. Song S.K., Sun S.W., Ju W.K., Lin S.J., Cross A.H. and Neufeld A.H., *Diffusion tensor imaging detects and differentiates axon and myelin degeneration in mouse optic nerve after retinal ischemia.* Neuroimage, 2003. **20**(3): p. 1714-22.
12. Henry R.G., Oh J., Nelson S.J. and Pelletier D., *Directional diffusion in relapsing-remitting multiple sclerosis: a possible in vivo signature of Wallerian degeneration.* J Magn Reson Imaging, 2003. **18**(4): p. 420-6.
13. Stanisz G.J., Kecojevic A., Bronskill M.J. and Henkelman R.M., *Characterizing white matter with magnetization transfer and T (2).* Magn Reson Med, 1999. **42**(6): p. 1128 36.
14. Laule C.,Vavasour I.M., Moore G.R., Oger J., Li D.K., Paty D.W. and MacKay A.L., *Water content and myelin water fraction in multiple sclerosis. A T2 relaxation study.* J Neurol, 2004. **251**(3): p. 284-93.
15. Springer F., Steidle G., Martirosian P., Claussen C.D. and Schick F, *Effects of in-pulse transverse relaxation in 3D ultrashort echo time sequences: analytical derivation, comparison to numerical simulation and experimental application at 3T.* J Magn Reson, 2010. **206**(1): p. 88-96.
16. Ernst R.R. and Anderson W.A. *Application of Fourier transform spectroscopy to Magnetic Resonance*. Rev Sci Instrum, 1966;**37**(1):93–102.
17. Jones C., MacKay A., and Rutt B., *Bi-exponential T2 decay in dairy cream phantoms.* Magn Reson Imaging, 1998. **16**(1): p. 83-5.

18. de Graaf Robin A. *In vivo NMR spectroscopy- Principles and Techniques*. 1998, John Wiley & Sons Ltd.
19. Bloch F, *Nuclear induction*. Phys Rev, 1946. **70**: 460-73.
20. Deoni S. C.L., Rutt B. K. and Peters T.M., *Rapid combined T1 and T2 mapping using gradient recalled acquisition in the steady state.* Magn Reson Med, 2003. **49**(3): p. 515 26.
21. Questions and answers in MRI. (2015, April 29). Retrieved from MRI Questions: **http://mri-q.com/spoiling---what-and-how.html.**
22. Springer F., Steidle G., Martirosian P., Syha R., Claussen C.D. and Schick F., *Rapid assessment of longitudinal relaxation time in materials and tissues with extremely fast signal decay using UTE sequences and the variable flip angle method.* Invest Radiol, 2011. **46**(10): p. 610-7.
23. Dieringer M.A., Deimling M., Santoro D., Wuerfel J., Madai V.I., Sobesky J., von Knobelsdorff-Brenkenhoff F., Schulz-Menger J. and Niendorf T., *Rapid parametric mapping of the longitudinal relaxation time T1 using two-dimensional variable flip angle magnetic resonance imaging at 1.5 Tesla, 3 Tesla, and 7 Tesla*. PLoS One, 2014. **9**(3): p. e91318.
24. Gupta Raj K., *Communication: A new look at the method of variable nutation angle for the measurement of spin-lattice relaxation times using Fourier transform NMR.* J Magn Reson, 1977. **25**:231-235.
25. Siversson C., Chan J., Tiderius C.J., Mamisch T.C., Jellus V. Svensson J. and Kim Y.J., *Effects of B1 inhomogeneity correction for three-dimensional variable flip angle T1 measurements in hip dGEMRIC at 3 T and 1.5 T.* Magn Reson Med, 2012. **67**(6): p. 1776-81.
26. Deoni, S. C.L., *High-resolution T1 mapping of the brain at 3T with driven equilibrium single pulse observation of T1 with high-speed incorporation of RF field inhomogeneities (DESPOT1-HIFI).* J Magn Reson Imaging, 2007. **26**(4): p. 1106-11.
27. Helms G., Dathe H., and Dechent P., *Quantitative FLASH MRI at 3T using a rational approximation of the Ernst equation.* Magn Reson Med, 2008. **59**(3): p. 667-72.
28. Helms G., Dathe H., Weiskopf N. and Dechent P., *Identification of signal bias in the variable flip angle method by linear display of the algebraic Ernst equation.* Magn Reson Med, 2011. **66**(3): p. 669-77.
29. Helms G. and G.E. Hagberg, *In vivo quantification of the bound pool T1 in human white matter using the binary spin-bath model of progressive magnetization transfer saturation.* Phys Med Biol, 2009. **54**(23): p. N529-40.
30. Zhang J., Kolind S.H., Laule C. and MacKay A.L., *Comparison of myelin water fraction from Multiecho T_2 decay curve and steady state methods.* Magn Reson Med, 2015. **73**(1): p. 223-32.
31. Bieri O. and Scheffler K., *On the origin of apparent low tissue signals in balanced SSFP.* Magn Reson Med, 2006. **56**(5): p. 1067-74.
32. Helms G., Dathe H., Kallenberg K. and Dechent P., *High-Resolution Maps of Magnetization Transfer with Inherent Correction for RF Inhomogeneity and T1 Relaxation Obtained from 3D FLASH MRI*. Magn Reson Med, 2008. **60**(6): p 1396–407.
33. Wansapura J.P., Holland S.K., Dunn R.S. and Ball WS JR. *NMR relaxation times in the human brain at 3.0 tesla.* J Magn Reson Imaging, 1999. **9**(4): p. 531-8.

8. Acknowledgements

I am very much indebted to my supervisor Gunther Helms for his supervision, guidance and constructive feedback during completion of this work. I not only enjoyed this project, but I also learned a lot of new things. I would also like to thank the MRI group in Lund, for motivating me and appreciating my work. I would like to especially thank my parents and my wife for their much appreciated support and encouragement that constantly gave me energy and strong will to continue my project despite difficulties and setbacks.